Title

TOWARDS A PRACTICAL IMPLEMENTATION OF THE MLE ALGORITHM FOR POSITRON EMISSION TOMOGRAPHY

Author

Llacer, J.

Publication Date

1985-10-01

Lawrence Berkeley Laboratory
UNIVERSITY OF CALIFORNIA

Engineering Division

Presented at the 1985 Nuclear Science Symposium, San Francisco, CA, October 21-25, 1985; and submitted to IEEE Transactions on Nuclear Science

TOWARDS A PRACTICAL IMPLEMENTATION OF THE MLE ALGORITHM FOR POSITRON EMISSION TOMOGRAPHY

J. Llacer, S. Andreae,
E. Veklerov, and E.J. Hoffman

October 1985

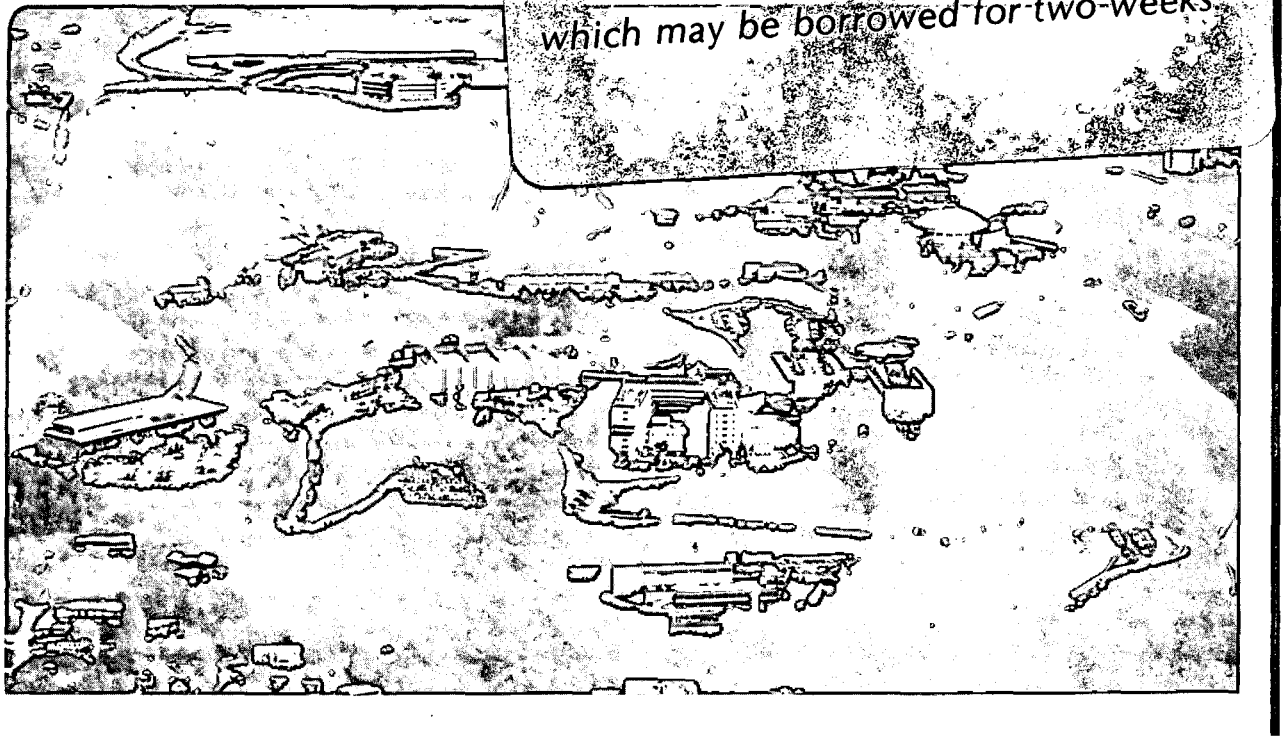

Prepared for the U.S. Department of Energy under Contract DE-AC03-76SF00098

DISCLAIMER

TOWARDS A PRACTICAL IMPLEMENTATION OF THE MLE ALGORITHM FOR POSITRON EMISSION TOMOGRAPHY

LBL-19668

Jorge Llacer, Sypko Andreae and Eugene Veklerov
Lawrence Berkeley Laboratory
University of California,
Berkeley, California 94720 U.S.A.
and
Edward J. Hoffman
Dept of Radiological Sciences, School of Medicine
University of California,
Los Angeles, California 90024 U.S.A.

ABSTRACT

Recognizing that the quality of images obtained by application of the Maximum Likelihood Estimator (MLE) to Positron Emission Tomography (PET) and Single Photon Emission Tomography (SPECT) appears to be substantially better than those obtained by conventional methods, we have started to develop methods that will facilitate the necessary research for a good evaluation of the algorithm and may lead to its practical application for research and routine tomography. We have found that the non-linear MLE algorithm can be used with pixel sizes which are smaller than the sampling distance, without interpolation, obtaining excellent resolution and no noticeable increase in noise. We have studied the role of symmetry in reducing the amount of matrix element storage requirements for full size applications of the algorithm and have used that concept to carry out two reconstructions of the Derenzo phantom with data from the ECAT-III instrument. The results show excellent signal-to-noise (S/N) ratio, particularly for data with low total counts, excellent sharpness, but low contrast at high frequencies when using the Shepp-Vardi model for probability matrices.

INTRODUCTION

The MLE algorithm described by Shepp and Vardi[1] for use in PET has recently received substantial attention due to its apparent ability to improve on the signal-to-noise (S/N) ratio of reconstructed images, in comparison with filtered backprojection methods.[2,3] The MLE algorithm has also been shown to provide improved images in the presence of scatter and attenuation effects in SPECT[4] and it has been demonstrated by Lange and Carson[5] that the MLE algorithm is also applicable to transmission tomography.

The main difficulty in attempting to implement the algorithm, even for the purpose of gaining some understanding of the characteristics of the reconstructed images, lies in the heavy demand that it places on computation resources. It is, therefore, not easy to study the benefits that could be derived from a routine use of that algorithm.

Since the quality of images and parameters derived from PET and SPECT measurements is generally limited by the number of photons that can be acquired in a given time interval, it is reasonable to expect that the MLE algorithm, based on the Poisson statistical nature of the photon emission process, would be the method of choice for image reconstruction and parameter estimation for those modalities. In order to ascertain whether that choice would be correct, we have considered it important to develop methods that facilitate an investigation of the capabilities and possible shortcomings of the MLE algorithm. We have started by implementing the algorithm for a small imaging system and continued with a progressive development of strategies for implementation with full size PET instruments. We will present here some results from point and line source reconstructions with a 96-crystal PET geometry and initial results of a 256 x 256 pixel reconstruction of the Derenzo phantom,[6] imaged by the ECAT-III device.[7] Strategies under development for large scale reconstruction will be described.

MATRIX FORM OF THE MLE ALGORITHM

The process of image reconstruction by the MLE algorithm has been described in a convenient matrix form recently by one of the present authors and co-worker.[8] That description will be repeated here with some improvements and it will provide the basis for the implementation strategies to be described below.

We consider each element of the image space to be an element of a vector X, whose value we want to estimate. Vector X will be of length Np (the number of pixels, for example). For the iterative MLE procedure, we will define X as the current estimate of the image vector and X' the new value after one more iteration.

As a result of a measurement, an imaging instrument will yield a vector of results K, of length Nc (the number of coincidences in a PET instrument, for example). The probability matrix A for the imaging instrument will have elements a(i,j) corresponding to the probability that a unit of activity at the jth pixel will give a response in the ith element of the results vector K. Matrix A will have Nc rows and Np columns and will be very sparse, in general.

We begin an iteration by defining a vector H of length Nc given by

$$H = A \; X \tag{1}$$

which corresponds to the results vector that the imaging instrument would yield if the true activity in the imaging space were X. H is, therefore, the projection of the current image estimate X, following the prescription given by matrix A, which defines the instrument.

We next define an error vector E with elements e(i) given by

$$e(i) = \begin{cases} k(i) \,/\, h(i) & \text{for } h(i) \neq 0 \\ 0 & \text{for } h(i) = 0 \end{cases} , \tag{2}$$

where k(i) and h(i) are the ith elements of vectors K and H, respectively.

The backprojection B of this error vector is obtained next as

$$B = A^T \; E \tag{3}$$

where A^T is the transpose of A. Then, the new image estimate is calculated as

$$x'(j) = x(j) \; b(j). \qquad (4)$$

It is then of advantage to repeat the operation of Eq. (1) and obtain a new value for H as

$$H' = A \; X' \qquad (5)$$

The change in likelihood for the iteration just completed can be calculated by the formula

$$dL = \sum_{i=1}^{Nc} [\, h(i)-h'(i)+k(i) \log(h'(i)/h(i)) \,] \qquad (6)$$

In principle, the iterative loop would be continued until dL has attained a desired low value.

The probability elements a(i,j) can be calculated in a number of ways. Shepp and Vardi have used a model in which a(i,j) is proportional to the width of the intersection of a circle inscribed in a pixel j and the ith strip joining two particular detectors.[1] For time-of-flight PET, Snyder and Politte have used asymmetrical, two-dimensional normal distributions, with appropriate variances along the line of flight and transverse to that line.[9] One of the present authors and coworkers, have used a program MATRIX[10] that calculates the probability elements for a two-plane multi-element positron emission camera by taking into account the characteristics of the detector material, dimensions and cross-talk between detector elements. Although Shepp and Vardi[1] mention that the results of their simulations are rather insensitive to the choice between two models that they have investigated, we feel that the calculation of probability matrix elements taking into consideration physical detector characteristics should become important with the advent of high resolution PET systems. At this time, however, we can only report results using the Shepp-Vardi model for probability calculations.

EXPERIMENTS WITH A 96-CRYSTAL RING

The geometry of the 96-crystal PET ring was described in a previous paper.[8] The measurements were carried out by rotations of two sets of 3 BGeO detectors (1.25 x 1.25 x 3 cm each) simulating the entire ring. A Na-22 line source of undetermined uniformity and approximately 0.078 μCi per cm and two Na-22 point sources of 1.1 and 0.185 μCi were imaged, collecting a total of 123,000 counts. In the previous paper we presented a comparison of the reconstructed images using the MLE algorithm and the fan-beam filtered backprojection technique. The images for the MLE algorithm were obtained by generating four 25 x 25 images and interleaving them for a total 50 x 50 pixel reconstruction. This interleaving was carried out in order to keep the distance between the centers of the pixels reconstructed in one single calculation larger than the sampling distance at the center of the ring (1.0 and 0.75 cm, respectively). The final 50 x 50 reconstruction had pixels of 0.5 x 0.5 cm. and the data were presented in a 128 x 128 interpolation. Figure 1a reproduces the results of that reconstruction, and Fig. 1b shows the filtered backprojection results. It was our experience with linear algebraic reconstruction methods that the condition number of the probability matrix A increases drastically as the pixel center-to-center distance approaches the sampling distance. This results in a strong increase in the RMS noise of a reconstruction[11,12] and should be avoided. We have found, however, that this caution appears unnecessary with the MLE algorithm, at least for point sources. Pixel size can be made much smaller than the sampling distance with apparent impunity. Using still the Shepp-Vardi model for probability functions, we have reconstructed the data for the line and point sources indicated above with one single matrix of 48 x 48 pixels, without interleaving and, further, with one single matrix of 96 x 96 pixels. In the latter case pixel size is 0.25 x 0.25 cm, still with a sampling distance of 0.75 cm. Figures 1c and Fig. 1d show the resulting images. Table I shows the width of the point response functions obtained.

TABLE I

Pixel size cm	Point response, cm, FWHM
0.5 x 0.5 (interleaved)	Approx. 1.1
.5 x 0.5 (single matrix)	" 0.8
0.25 x 0.25 (single matrix)	" 0.6

No visible increase in the noise in background areas was observed.

RECONSTRUCTIONS FROM THE ECAT-III TOMOGRAPH

The ECAT-III tomograph[7] is an instrument with 512 crystals in each of two rings with a detector diameter of 100 cm, and a patient opening of 65 cm. Resolution is 4-5 mm with wobbling and 5-6 mm without. For non-wobbling operations and a single ring, the number of allowed coincidences Nc for the data being analyzed is 49152 (512 angles with 96 bins each). An image plane with Np=65536 (256 x 256 pixels) has been used for the MLE reconstructions. Considering that each pixel is of dimensions 0.1016 x 0.1016 cm and that each of the projection bins is as wide (at the center region) as the detector center-to-center distance (0.61 cm), it is clear that each column of the probability matrix A will have, at most, two non-zero elements per angle, or a maximum of 1024 non-zero elements. For 65536 columns, the number of non-zero elements that we need to store is 67 million, each consisting of one integer address and one floating point value, or 6 bytes. Total required storage space is then 402 Mbytes, a number which is prohibitive for an initial research effort with general purpose medium size computers.

Fortunately, for a tomograph with a number of detectors which is a multiple of 8 and a square image region, eight-fold symmetry exists in the detector-pixel assembly. The matrix elements for a particular pixel are repeated in 3 or 7 other sectors of the A matrix (depending on whether the pixel is on a diagonal or off-diagonal) and can be retrieved by proper symmetry operations. By implementing routines to carry out the products of Eqs. (1) and (3) using the smaller matrices, we have reduced storage to approximately 51 Mbytes, a figure that is more reasonable than the initial 402 Mbytes.

The MLE reconstructions shown in this paper have been carried out by the 8-fold symmetry procedure, using probability matrix elements calculated from the Shepp-Vardi model, as discussed above.

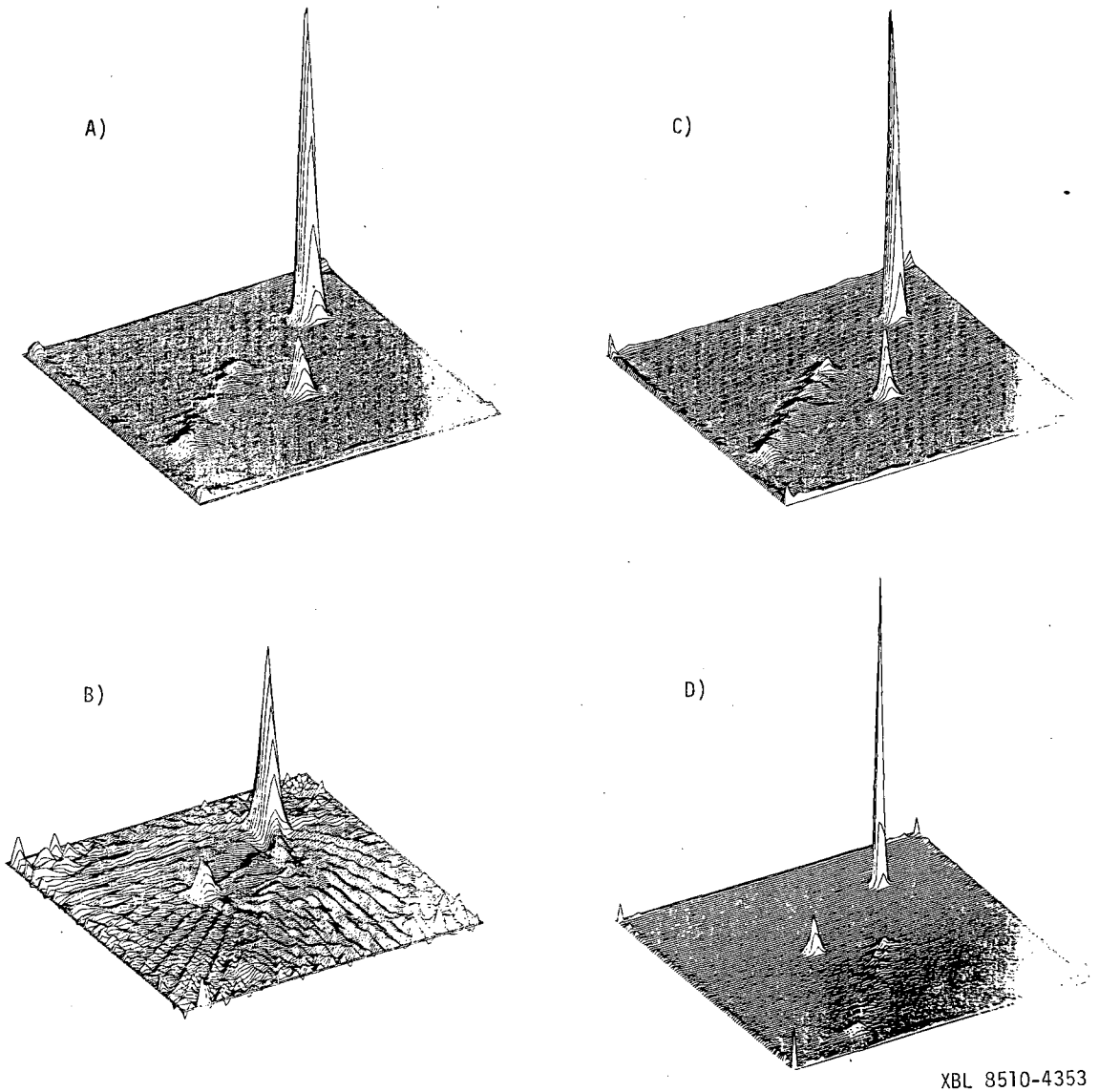

Figure 1. Results of image reconstruction using rotating BiGeO crystals in a 96-crystal configuration, with point and line sources. Shepp-Vardi model for probability matrix elements. a) Four interleaved sets of pixels, for a total 50 x 50 image. b) Image obtained using the fan beam filtered backprojection technique, with 50 x 50 pixels. c) MLE reconstruction with 48 x 48 pixels, without interleaving. Pixel size is 0.5 x 0.5 cm, sampling distance is 0.75 cm. d) MLE reconstruction with 96 x 96 pixels, no interleaving. Pixel size is 0.25 x 0.25 cm, sampling distance 0.75 cm.

We have reconstructed images of the Derenzo phantom[6] filled with F-18. The phantom contains cylinders of activity with diameters ranging from 2.5 to 6.25 mm in a circle of 20 cm. Two images have been reconstructed, one with 40 million net true events and one with 0.6 million events. Accidentals rate was kept below 15% during data collection and they have been subtracted. Data were corrected for attenuation losses by a simple multiplicative method. A total of 45 iterations has been obtained for each of the two reconstructions and the results can be compared to filtered backprojection images obtained with ramp and Hanning filters.

Figure 2 shows the values of the change in likelihood function dL of Eq. 6 as a function of iteration number for the two reconstructions. The function dL is the derivative of the likelihood function, which normally exhibits a saturation behavior. The likelihood function L is the logarithm of the function that expresses true likelihood[1] and, therefore, the saturation behavior of L is expected. Plotting dL in a semilog scale allows us to observe the behavior of convergence, or non-convergence, better than by observation of L. For both reconstructions we observe that up to iteration No. 10, approximately, likelihood has increased quite rapidly, but after that it increases at a slower rate. At the end of

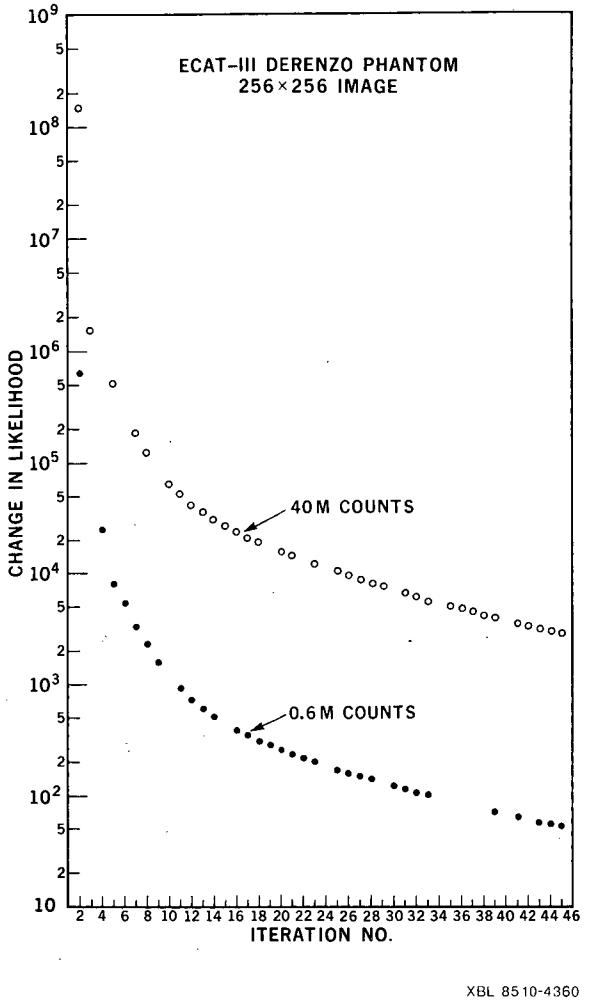

Figure 2. Change in likelihood functions (dL, Eq. 6) for the two reconstructions of the Derenzo phantom as a function of iteration number. Points missing correspond to interations in which the function was not calculated.

the 45 iterations that we have carried out we are still increasing in likelihood, although the increases are in a region of negative exponential form. We plan to continue the present iterative process with the two images after we develop more efficient programs, as discussed below, in order to see whether dL keeps following the negative exponential behavior of Fig. 2 or, at some point it drops more rapidly again, indicating no further increase in likelihood.

Figure 3 shows the image obtained from the 40 million count data by the ramp and Hanning filters, and at iteration No. 45 by the MLE algorithm. Similarly Fig. 4 shows the results for the 0.6 million count data. The figures also indicate the standard deviation of the noise (in ct numbers) in the circular regions shown in Fig. 5 at the center of the phantom and at the periphery. Notice that the display scale for the MLE results has been expanded by a factor of two with respect to the ramp and Hanning filter images, so that any existing noise would appear more prominently.

Figure 6 shows cuts along the 3 lines shown in Fig. 5 for the ramp, Hanning and MLE images for the 40 Mcount data. Results for iterations 15, 27 and 45 are shown for the MLE case. Figure 7 shows cuts for the 0.6 Mcount data.

DISCUSSION OF RESULTS

The results of Figs. 3 to 7 can be summarized by separating some of the more important elements that contribute to image quality: Signal-to-noise ratio (S/N), contrast, frequency response, accuracy of shape and signal magnitude, distortions and artifacts. Since the MLE is a non-linear algorithm, some of the image characteristics that would be related in linear methods may be independent here. For the present preliminary reconstructions we will examine only the more salient features of the images in terms of some of the image characteristics indicated.

S/N

With the images normalized so that the highest signal fills 1024 ct numbers, we find the ratios for S/N of the MLE vs the filtered backprojection techniques shown in Table II.

TABLE II

Comparative S/N ratios with Shepp-Vardi probability matrices

	40 Mcounts		0.6 Mcounts	
	Center	Outer	Center	Outer
$S/N_{MLE}/S/N_{ramp}$	3.84	6.66	7.69	25.0
$S/N_{MLE}/S/N_{Hanning}$	2.56	4.54	15.38	50.0

The above figures are obtained by dividing the reciprocals of the two noise standard deviations in the corresponding circular regions indicated in Fig. 5. Evidently, the figures are only meaningful in comparing methods with identical frequency response and we do not have that case here. For that reason we shall examine contrast next, as some indication of frequency response, and relate the above results to the new findings.

Contrast

We can define contrast for the four regions of the Derenzo phantom described by lines PL1 and PL2 of Fig. 5 as the normalized average distance between peak and valley along those lines for the 40 Mcount data. Table III shows the results obtained.

TABLE III

Comparative contrast values using the Shepp-Vardi probability functions

Region	Source diameter	Source separation	CONTRAST Ramp	Hanning	MLE
1	6.25 mm	25 mm	Defined as 1.00		
3	4.00	16	0.41	0.39	0.21
4	3.50	14	0.31	0.31	0.18
6	2.50	10	0.16	0.05	0.04

Finally, we show the region dependent comparative S/N ratios assuming that contrast remains fixed at the 40 Mcount values when the total number of counts in the image changes and noise is uniform within the activity region of the Derenzo phantom and equal to the center circular region (Fig. 5). The values obtained are shown in Table IV and result from modifying those of Table II by the ratios of contrasts in Table III.

We emphasize that the results in Tables II through IV are for the Shepp-Vardi model for probability values. We feel that the choice of a model that represents realistically the physics of detection may improve the S/N figures substantially, particularly at higher frequencies.

TABLE IV

Comparative region dependent S/N ratios with Shepp-Vardi probability matrices

	40 Mcounts				0.6 Mcounts			
Region:	1	3	4	6	1	3	4	6
$S/N_{MLE}/S/N_{ramp}$	3.84	1.96	2.22	0.96	7.69	3.93	4.46	1.96
$S/N_{MLE}/S/N_{Hanning}$	2.56	1.37	1.48	2.05	15.4	8.3	8.9	12.3

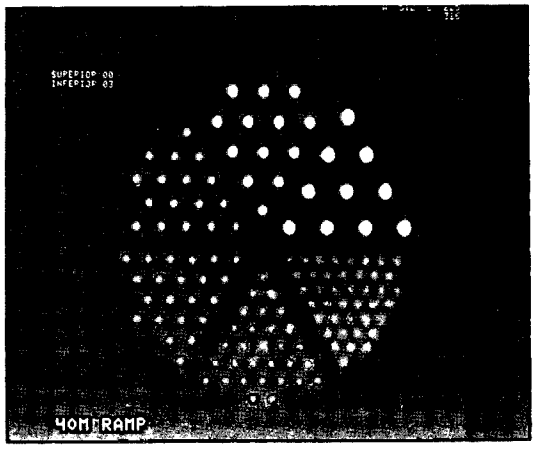

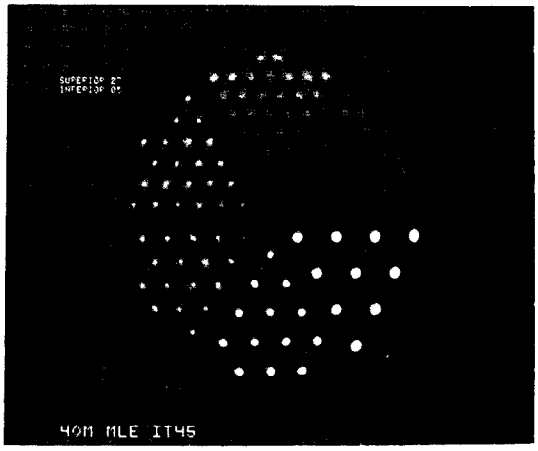

Comparison of Derenzo Phantom Images, ECAT-III Data, Non-Wobbling.

40 Million Counts

Method	Center Region Noise	Outer Region Noise	Range Displayed
Ramp filter	Std. dev. = 10.7 ct nos.	Std. dev. = 4.8 ct nos.	0-1024 ct nos.
Hanning filter	7.2	2.7	0-1024
MLE, 45 iters.	2.8	0.6	0-512

Figure 3. Comparison of images obtained with 40 Mcounts with Ramp and Hanning filtered backprojection techniques and at iteration 45 of the MLE algorithm. (Shepp-Vardi probability matrices).

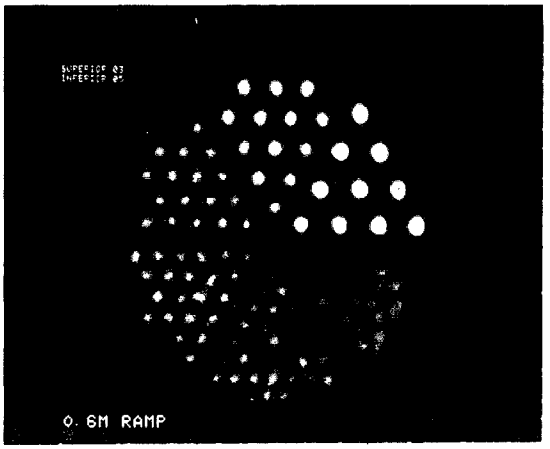

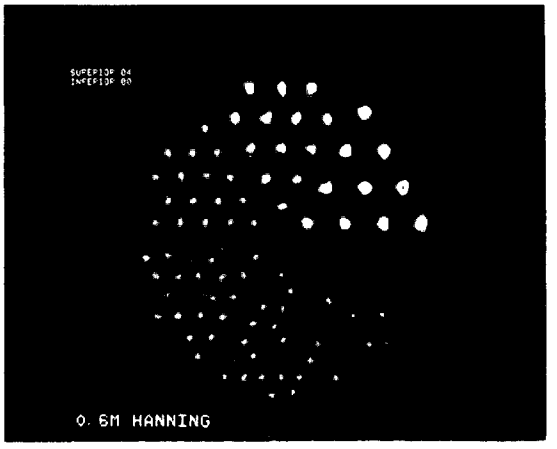

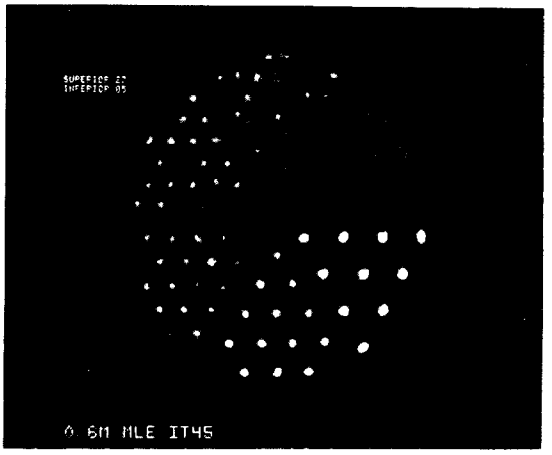

Comparison of Derenzo Phantom Images, ECAT-III Data, Non-Wobbling.

0.6 Million Counts

Method	Center Region Noise	Outer Region Noise	Range Displayed
Ramp filter	Std. dev. = 20.3 ct nos.	Std. dev. = 10.0 ct nos.	0-1024 ct nos.
Hanning filter	40.0	20.8	0-1024
MLE, 45 iters.	2.6	0.4	0-512

Figure 4. Similar comparison as in Fig. 3, for 0.6 Mcounts.

Frequency response

The concept of frequency response should be related in some manner to the contrast figures shown in Table III but that relationship is not clear from the present initial reconstructions. Although we found the MLE algorithm to show lower constrast for the regions with sources of smaller diameter than with the ramp filter reconstruction, the sharpness of the 6.25 mm diameter sources (Region 1) is better reproduced by the MLE algorithm: the ramp filter shows approximately 7 mm FWHM and 12.2 mm FW1/10M while the MLE results show 4.5 mm FWHM and 7.7 mm FW1/10M. We should point out that the MLE reconstruction has been carried out with 1.016 x 1.016 mm pixels, in clear violation of the sampling theorem. The filter used for the ramp reconstructions was for the 3.05 mm sampling distance, with interpolation to a 256 x 256 image plane during backprojection.

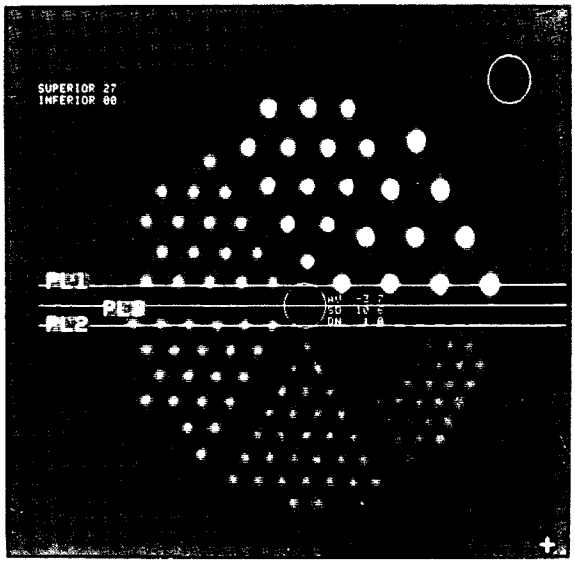

Figure 5. Lines for the cuts of Figs. 6 and 7 and circles for noise data in Table II.

FURTHER DEVELOPMENT OF STRATEGY

The continuation of the research described above with data from practical devices like the ECAT-III will depend on the availability of substantial computation resources which should be used in a most efficient manner. The reduction of matrix elements by using 8-fold symmetry is a step in the right direction, although it results in longer computation times because of the transformations required for the matrix products. This added computation time

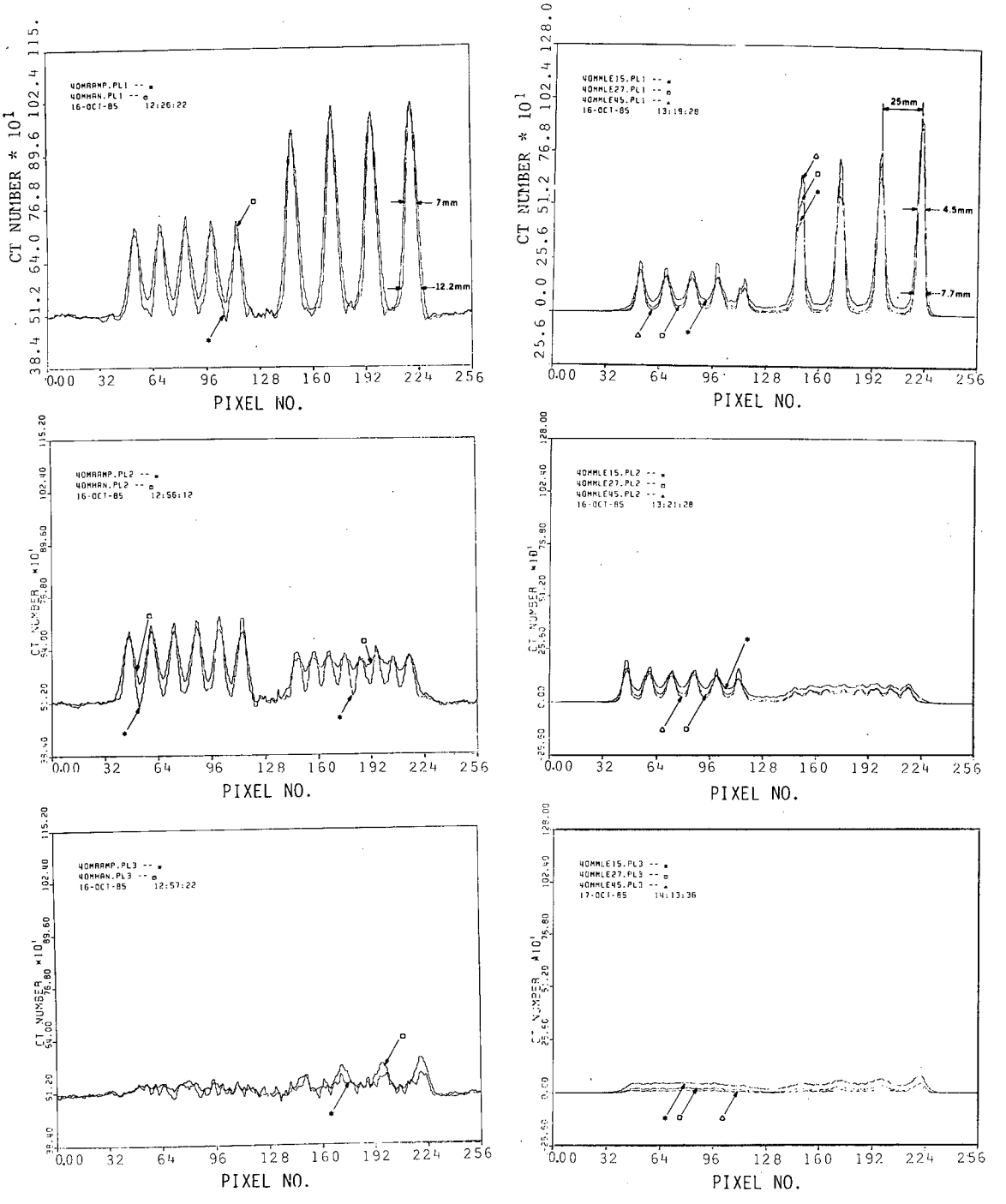

Figure 6. Cuts along lines PL1, PL2 and PL3 indicated in Fig. 5, for the 40 Mcount reconstructions.

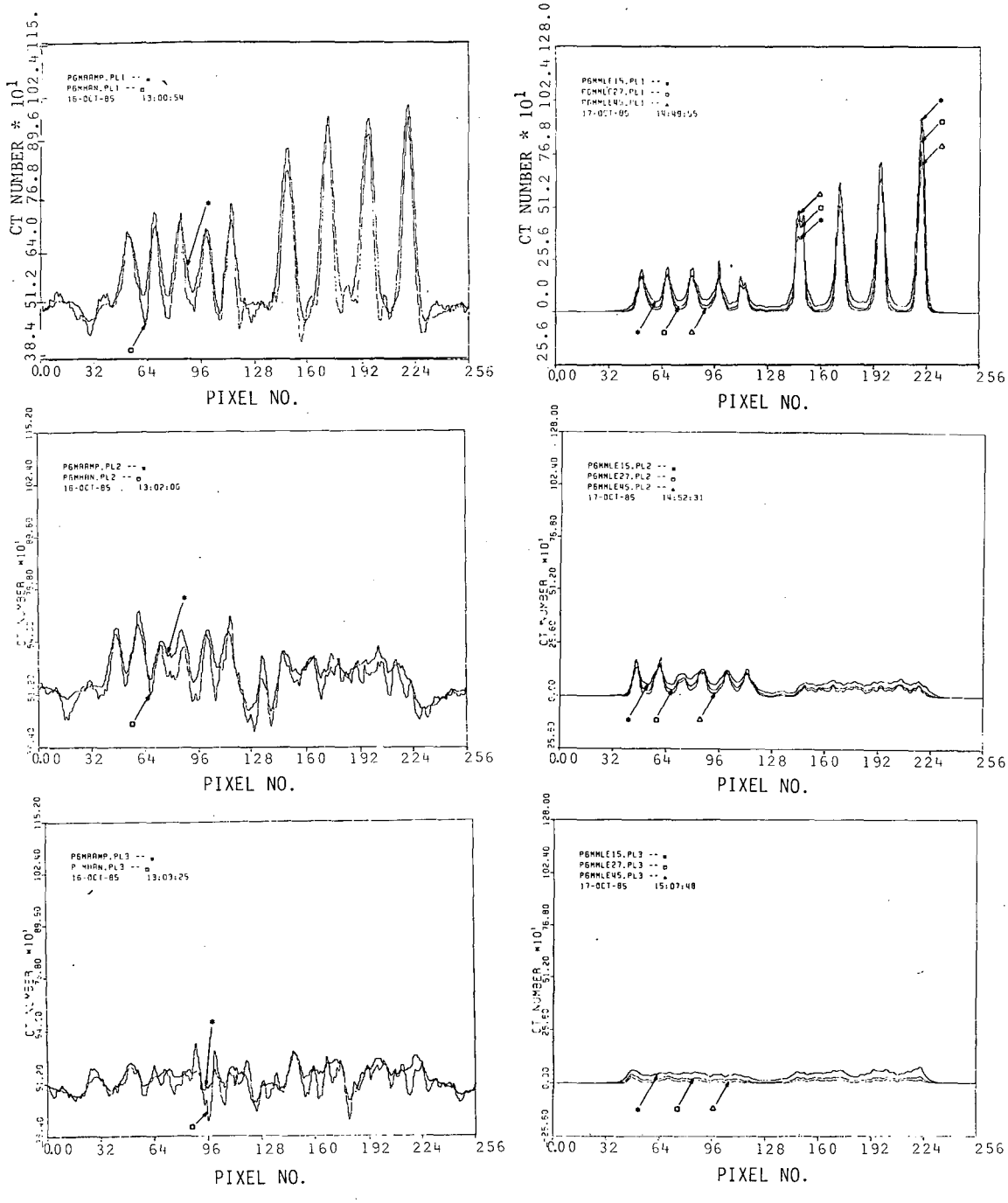

XBL 8510-4362

Figure 7. Cuts for the same lines as in Fig. 6, for 0.6 Mcounts.

can be shortened considerably by making some important changes to the computation procedure, which, at this time, is still rather unsophisticated. The changes that are contemplated for the immediate future are:

1) In carrying out the matrix products of Eqs. (1) and (3), a number of dot products (4 or 8) can be carried out for each column of the A matrix read from disk, corresponding to all equivalent pixels.

2) The body of the main iteration can be modified to avoid repeated operations. We can consider iterating a loop represented by Eqs. (2) to (5), with Eq. (1) being a preamble. In that manner, Eqs. (3),(4) and (5) can be calculated by reading each column of the truncated A matrix only once and carrying out the transformations only once also. This becomes clear by the following considerations:

a) Let's assume we read column j of matrix A corresponding to a particular pixel. With vector E available, we carry out the dot product

$$b(j) = \sum_i a(i,j)\ e(i) \quad . \qquad (7)$$

The new image element x'(j) can then immediately be calculated from Eq. (4) with the value b(j) just obtained. We proceed by incrementing each value h'(i) with the contribution of x'(j) and the same matrix column values a(i,j) still available in the main computer memory, i.e.,

for all i, increment h'(i) by

$$a(i,j)\ x'(j). \qquad (8)$$

After completing the above operations for column j, corresponding to one pixel, we carry out the needed transformations to define another pixel that has the same values a(i,j) already available in main memory (except for reflection operations) and proceed with the partial matrix products indicated. This is followed by the operations for another equivalent pixel, etc.

In this manner the number of read operations from disk is kept to a miminum and the transformation calculations (which half the time involve reversing the order of the matrix elements corresponding to specific projections) are also not duplicated.

3) Using very compact code in the matrix product and transformation operations. It will be necessary to investigate the most favorable language for writing the program sections that are most often repeated. It may necessary to code some loops in assembly language for maximum efficiency.

4) Investigate methods of double buffering, by which the main computer cpu is carrying out calculations with one set of matrix elements while matrix read operations are carried out with another set of elements.

5) Investigate possible cpu time savings by using fixed point instead of floating point arithmetic for the main repeated loops.

Essentially, it appears necessary to approach the coding of the MLE algorithm with substantial care and sophistication, avoiding simple straight forward code which, in this case, results in prohibitive computation times for anything but a first look at the algorithm. With the improvements outlined above, we expect cpu times of approximately 45 minutes per iteration for a VAX-780 computer for the ECAT-III problem, without wobbling. That level of performance can make research on the characteristics of the algorithm feasible, although a full scale implementation for routine image reconstruction would need a dedicated multiprocessor system, as we have outlined in a previous paper.[8]

CONCLUSIONS

We have examined the results of some preliminary MLE reconstructions with a small detector system. The outcome of those reconstructions was found to be encouraging and has led us to develop a strategy that would allow us to carry out full scale reconstructions. While we are developing that strategy, we have been able to carry out two reconstructions with up to 45 iterations each that continue showing excellent S/N ratios, particularly for images with limited number of counts, good sharpness for the larger diameter sources of the Derenzo phantom, although lower contrast ratios than the ramp reconstruction. A large amount of work remains to be done in order to fully evaluate the technique. That work should include the generation of probability matrices that reflect more closely the detection process, the development of sophisticated programs that use computer operating systems and machine instructions efficiently and the reconstruction of data from a variety of source shapes and contrats ratios, including normal and abnormal clinical images.

ACKNOWLEDGEMENTS

The authors would like to thank A. Chatterjee for his support for this work and D. Rondeau and R. P. Singh for their help in finding a computer on which the preliminary computations described in the paper could be carried out.

This work was supported in part by the National Cancer Institute (CA-27021) and the Office and Environmental Resources of the U.S. Department of Energy under Contract No. DE-AC03-76SF00098. Reference to a company or product name does not imply approval or recommendation of the product by the University of California or the U.S. Department of Energy to the exclusion of others that may be suitable.

REFERENCES

1. L.A. Shepp and Y. Vardi, "Maximum Likelihood Reconstruction for Emission Tomography", IEEE Trans. Med. Imaging, MI-1, No. 2, pp 113-121, 1982.

2. D.G. Politte and D.L. Snyder, "Results of a Comparative Study of a Reconstruction Procedure for Producing Improved Estimates of Radioactivity Distributions in Time-of-Flight Emission Tomography", IEEE Trans. Nucl. Sci., NS-31, No. 1, pp 614-619, 1984.

3. L.A. Shepp, Y. Vardi, J.B. Ra, S.K. Hilal and Z.H. Cho, "Maximum Likelihood PET with Real Data", IEEE Trans. Nucl. Sci., NS-31, No. 2, pp 910-913, 1984.

4. C.E. Floyd, R.J. Jaszczak and R.E. Coleman, "Inverse Monte Carlo: a Unified Reconstruction Algorithm for SPECT", IEEE Trans. Nucl. Sci., NS-32, No. 1, pp 779-785, 1985.

5. K. Lange and R. Carson, "EM Reconstruction Algorithms for Emission and Transmission Tomography", J. Comp. Assisted Tomography, pp 306-316, April 1984.

6. S.E. Derenzo, T.F. Budinger, J.L. Cahoon, R.H. Huesman and H.G. Jackson, "High Resolution Computed Tomography of Positron Emitters", IEEE Trans. Nucl Sci., NS-24, No. 1, pp 544-558, 1977.

7. E.J. Hoffman, A.R. Ricci, L.M.A.M. Van der Stee and M.E.Phelps, "ECAT III, Basic Design Considerations", IEEE Trans. Nucl. Sci., NS-30, No. 1, pp 729-733, 1983.

8. J. Llacer and J.D. Meng, "Matrix-Based Image Reconstruction Methods for Tomography", IEEE Trans. Nucl. Sci., NS-32, No. 1, pp 855-964, 1985.

9. D.L. Snyder and D.G. Politte, "Image Reconstruction from List-Mode Data in an Emission Tomography System Having Time-of-Flight Measurements", IEEE Trans. Nucl. Sci., NS-20, No. 3, pp 1843-1849, 1983.

10. J. Llacer, A. Chatterjee, E.K. Batho and J.A. Poskanzer, "Design Analysis and Performance Evaluation of a Two-Dimensional Camera for Accelerated Positron Emitter Beam Injections by computer simulation", IEEE Trans. Nucl. Sci., NS-26, No. 1, pp. 596-602, 1979.

11. Llacer, "Theory of Imaging with a Very Limited Number of Projections", IEEE Trans. Nucl. Sci., NS-26, No. 1, pp 596-602, 1979.

12. J. Llacer, "Tomographic Image Reconstruction by Eigenvector Decomposition: its Limitations and Areas of Applicability", IEEE Trans. Med. Imaging, MI-1, No. 1, pp 34-42, 1982.

TECHNICAL INFORMATION DEPARTMENT
LAWRENCE BERKELEY LABORATORY
UNIVERSITY OF CALIFORNIA
BERKELEY, CALIFORNIA 94720